Measurement Science
and Technology

PURPOSE-LED
PUBLISHING™

PAPER • **OPEN ACCESS**

A small robust monolithic vacuum-compatible microbalance with automated calibration: achieving high accuracy with a large load capacity

To cite this article: R F M Martens *et al* 2025 *Meas. Sci. Technol.* **36** 045004

View the article online for updates and enhancements.

You may also like

- Evaluation of InGaAs and InP Compatibility with Alkaline Photoresist Stripping Formulations
Glenn Westwood
- Magnetic Sample Environment for in-situ SAXS/WAXS Measurements on Magnetic Nanoparticles with Shape Anisotropy
D Skroblin, L Cibik, B Klemke et al.
- Development and construction status of the Mu2e electromagnetic calorimeter mechanical structures
N. Atanov, V. Baranov, L. Borrel et al.



This content was downloaded from IP address 15.204.172.40 on 11/11/2026 at 12:55

OPEN ACCESS
IOP Publishing
Measurement Science and Technology
Meas. Sci. Technol. **36** (2025) 045004 (19pp)
https://doi.org/10.1088/1361-6501/adbc07

A small robust monolithic vacuum-compatible microbalance with automated calibration: achieving high accuracy with a large load capacity

R F M Martens, O van der Sluis, M G D Geers and J P M Hoefnagels*

Department of Mechanical Engineering, Eindhoven University of Technology, Eindhoven, The Netherlands

E-mail: j.p.m.hoefnagels@tue.nl

Received 23 September 2024, revised 14 January 2025
Accepted for publication 3 March 2025
Published 20 March 2025

Abstract

The increasing demand for compact and efficient electronics has led to the miniaturization of components such as microchips, sensors, batteries, and storage devices. As these dimensions decrease, monitoring mass changes becomes essential for controlling the various physical processes involved in manufacturing, including material addition or removal during physico-chemical steps like thin-film micro-fabrication (e.g. depositing, patterning, doping, etching, surface oxidation/nitridation). This need has triggered the development of diverse microbalances. While custom-made setups typically aim for high resolution and large load capacity, they are difficult to construct, fragile, and consume significant space. On the one hand, quartz sensors, which measure weight changes through resonance frequency, offer high resolution and load capacity in a compact footprint, but for multiple reasons their applicability is limited to the deposition of a thin film directly onto the quartz sensor. On the other hand, commercial microbalances allow loose sample placement but lack vacuum compatibility. To address these limitations, a new robust vacuum-compatible monolithic microbalance has been devised, relying on the design of a dedicated elastic mechanism that achieves a resolution below one microgram for loads exceeding one gram. This balance is manufactured using electrical discharge machining and micromilling, resulting in a small, sturdy device with an automatic in-situ calibration mechanism. The resulting microbalance is optimized for deposition and etching processes, ensuring accurate measurements in a wide range of challenging vacuum environments. The novelty of the microbalance lies in its unique combination of features: high accuracy ($<1\,\mu$g), high sensitivity ($<0.1\,\mu$g), large load capacity (>1 g), a compact footprint ($\approx 30 \times 30 \times 10$ cm^3), high robustness ($\approx$30 g) due to its built-in mechanical stops, vacuum compatibility, and compatibility with depth profile analyses.

Keywords: mass monitoring, microbalance, deposition and etching processes, In-situ calibration, elastic mechanism, electrical discharge machining

* Author to whom any correspondence should be addressed.

Original Content from this work may be used under the terms of the Creative Commons Attribution 4.0 licence. Any further distribution of this work must maintain attribution to the author(s) and the title of the work, journal citation and DOI.

© 2025 The Author(s). Published by IOP Publishing Ltd

1. Introduction

As the demand for smaller and more efficient electronics grows, the components that power these devices are shrinking [1–4]. Transistors, capacitors, inductors and resistors, now smaller than ever, require increasingly precise application and manipulation of thin films using increasingly advanced processing techniques such as atomic layer deposition [5–8]. Therefore, as these dimensions decrease, accurate monitoring of the mass change becomes increasingly important for controlling the material addition and removal during the wide range of physico-chemical processing steps (deposition, patterning, doping, etching, surface oxidation/nitridation, cleaning, etc) involved in micro-fabrication of microelectronics and MEMS [9–13]. The ability to measure such small weight variations enables optimization of the reliability and performance of the next generation of electronic devices [14–18], but it requires a dedicated microbalance designed to detect minute weight changes in challenging vacuum environments, e.g. the harsh plasmas used for deposition and etching. Additionally, highly accurate mass measurement could advance depth profile analyses of the finished product, i.e. the wafers with multilayer stacks. In such analyses, the final multilayer stack is removed layer by layer, using a focused ion beam or etch plasma, while monitoring with a sensitive diagnostic, such as x-ray photoelectron spectroscopy, secondary ion mass spectrometry, auger electron spectroscopy, glow discharge optical emission spectroscopy, electron back-scatter diffraction, or wafer-curvature stress sensing. Because nanometer resolution measurement of the thickness of a multilayer stack is typically not possible [19–22], a microbalance could be used to measure the weight change which is converted to a thickness change using the density of the removed material. As detailed below, the presently existing microbalances are not suited for *in-situ* monitoring of minute mass changes in these circumstances, either during micro-fabrication processing or layer-by-layer depth profiling. To this end, this paper introduces a new, robust, easy-to-handle monolithic microbalance with 0.1 μg accuracy for loads up to 2 grams and with automated *in-situ* calibration that warrants accuracy in challenging vacuum environments.

Microbalances are instruments that detect very small force changes below 10^{-7} N [23] corresponding to a mass a less than 10 μg. Microbalances are widely used in various scientific and industrial applications [24]. Until 1960, microbalances were originally custom-built, but thereafter, commercially available microbalances became prevalent. Various microbalances nowadays exist, each with its advantages and disadvantages. The most common microbalances can be classified into four categories based on their working principle: the quartz microbalance, the cantilever microbalance, the spring microbalance, and the beam microbalance [25]. Figure 1 summarizes the main advantages and disadvantages of the different microbalances, as discussed next.

The first category, the quartz crystal microbalance (QCM), consists of a quartz crystal, which is electrically driven by an oscillator to determine the eigenfrequency of the crystal [26, 27]. Deposition of a thin film on the quartz crystal alters its eigenfrequency, which is converted to a mass change. QCMs are capable of detecting mass changes at the picogram level making them the most sensitive, while they have high-temperature stability and can operate in various environments, including vacuum, gas, and liquid phases. For instance, QCMs are successfully employed to monitor the mass increase during thin film deposition on a substrate [28], by placing a QCM close to the substrate, assuming uniform deposition on the substrate and crystal. But there are limitations. The assumption of uniform deposition is not always valid, while the maximum layer thickness is typically limited to a few hundred nanometers up to several microns, depending on the film's rigidity [29–31]. Moreover, realistic deposition of a multi-layer stack on the QCM crystal is generally not possible as only standard silicon wafers are accepted in the various high-end micro-fabrication process tools [32–34]. Finally, a critical requirement of QCMs is a perfect connection between the mass to be weighted and the quartz crystal [35]. The required solid connection and limitation to micron-thin specimens prevent QCMs to be used as a conventional weighing scale onto which a separate wafer with thin film or multi-layer stack can be placed. These limitations make QCMs also unsuited for precise depth profile measurements of finished wafers with a multilayer stack that is removed layer by layer while being analyzed with an advanced diagnostic, as discussed above.

The second category is the cantilever microbalance, which is the simplest microbalance and has a small footprint. A weight is placed at the free end of a cantilever, and the deflection is converted into a change of mass [36]. Alternatively, the mass change can also be determined by monitoring the change in the eigenfrequency of the cantilever, but this would also require a solid connection between the sample and the cantilever [37]. Cantilevers can be optimized to measure forces in the pico-Newton-regime [38]. However, cantilevers are fragile due to their long slender structure. If not handled carefully, they easily plastically deform or fail, even when they are not weighing a sample [39]. Moreover, they have the lowest load capacity to resolution ratio. Therefore, this method is not applicable to relatively heavy samples in the range of 1 g, such wafer curvature specimens, that must be measured with a high accuracy of, for example, 1 μg.

The third category is the spring microbalance. The simplest form is a helical spring extending proportionally to the applied load. A spring microbalance is cheap and easy to produce but is sensitive to vibrations, has a low load capacity to resolution ratio, and should be thermostatted to achieve an accurate reading [40].

The last category is the beam microbalance, which consists of a beam attached to a fulcrum at its center [24, 41, 42]. The sample is placed on one beam end, and the counterweight is on the opposite side. A change in the sample weight causes a change in moment, which induces a rotation of the fulcrum. Beam microbalances are categorized by the fulcrum type: knife edge, torsional, and pivotal [43]. The

	Load Capacity to Resolution Ratio	Vacuum Compatible	Robustness	Footprint	Backside Optical Diagnostics	Substrate Choice	Applicable for material removal
Quartz Crystal Microbalance	+	++	++	++	- -	- -	- -
Cantilever Microbalance	- -	++	- -	++	-	++	+
Spring Microbalance	- -	+	-	++	+	++	+
Modern designs Beam Microbalance	++	+	- -	- -	+	++	+
Commercially Available Microbalance	++	- -	+	-	-	++	–
Novel monolithic beam microbalance	+	++	++	++	++	++	++

Figure 1. Specifications of various existing microbalance techniques, along with the newly proposed monolithic beam microbalance, are outlined. The color scheme used indicates the following: light green (+) represents full compliance with the requirements, dark green (++) indicates performance exceeding the requirements, orange (–) signifies the need for significant design modifications to meet the requirements, and red (– –) indicates that the requirements cannot be fulfilled.

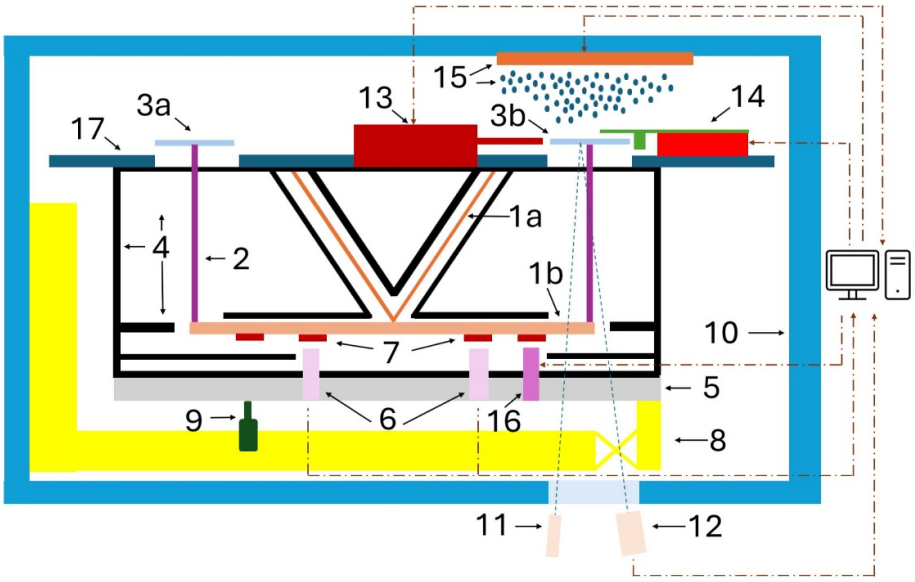
knife edge is preferred for heavy samples above 20 g. The torsional microbalance is preferred if the highest resolution is needed, while the pivotal beam microbalance is the most rugged microbalance and the least sensitive to vibrations [25]. Beam microbalances can achieve a very high load capacity to resolution ratio, but the traditional beam microbalances before 1970 all are difficult to manufacture, fragile, and have a large footprint [23, 24, 44].

Nowadays, most commercially available microbalances are based on beam microbalances [45]. Their design has been improved by implementing a flexure-based four-bar linkage and a lever mechanism in combination with an electromagnetic actuator, as explained in [46], resulting in microbalances with a resolution below 1 μg and with a load capacity of up to 6 g [47, 48]. They are optimized for use at atmospheric pressure, have a relatively small footprint, and their design has been upgraded to be less fragile than the traditional beam microbalances [43, 48]. A control loop corrects for temperature variations and electrostatic charges. However, commercial microbalances have various design features that make them unsuitable for use in vacuum conditions. The weigh module is encapsulated and sealed with silicone. In vacuum, this seal breaks, exposing the weigh module to ambient conditions, causing drift that significantly reduces the accuracy [43]. Moreover, the vacuum affects the long-term stability of the zero-point of the microbalance [49]. Besides, commercial microbalances utilize high-precision motors that rely on special bearings made of sintered metal filled with oil to achieve accurate auto-calibration and auto-leveling of the microbalance [50]. In a vacuum, the oil evaporates over time, contaminating the vacuum chamber and reducing the motor accuracy [49]. It can thus be concluded that to achieve an optimal beam microbalance for vacuum applications, a new design following a different design philosophy is required.

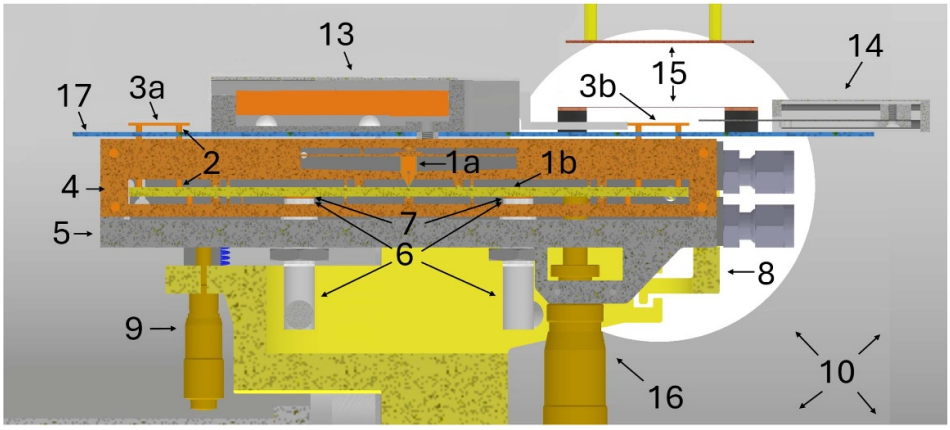
Therefore, this paper presents the design, manufacture, and calibration of a new microbalance with a capacity of 2 g and an accuracy of 1 μg. The balance is compatible with optical diagnostics and the challenging vacuum and plasma environment conditions. It has been designed for high robustness against failure, a small footprint to fit in the vacuum chamber, and insensitivity to uniform temperature changes. Meeting these requirements, the microbalance will also be suitable for monitoring thin-film microfabrication and analysis processes where a quartz crystal cannot be installed. To achieve this, we will propose a novel design, validate its sensitivity using Finite Element Analysis (FEA), and optimize it accordingly. A novel manufacturing methodology involving computer-controlled subtractive methods will be employed, resulting in a robust, monolithic microbalance. Auxiliary parts will be developed to automate experiments, minimize temperature gradients and vibrations, and extend the microbalance's range. Additionally, a dedicated calibration system will be devised for automatic calibration.

2. Specifications and overview of the new microbalance design

The microbalance has been developed as a generic device for monitoring mass changes in vacuum processes with a resolution below $\approx 1\,\mu$g, which is sufficient to monitor most physico-chemical reactions and processes during the thin-film micro-fabrication steps [51]. The target specimens are thin films or multilayer stacks on a silicon wafer with an approximate length and width of $\approx 10 \times 10$ cm^2, weighing a few milligrams. A larger specimen size increases the thickness accuracy, however, it also makes achieving high uniformity in processing (etching, deposition, etc) increasingly difficult. For these in-plane specimen dimensions, a thickness accuracy of 1 nm corresponds to a required weight accuracy of at least 1 μg. Additionally, the microbalance design has been optimized not only for compatibility with vacuum and plasma environments but also for maximum robustness against plastic deformation or failure. Moreover, it has been designed to be small enough to allow easy installation by replacing the sample holder in vacuum deposition and etching systems, which typically requires a footprint below $\approx 30 \times 30$ cm^2 and a height below ≈ 10 cm [52]. Moreover, the microbalance has been designed to be compatible with optical diagnostics accessing the bottom of the specimen, such as a wafer-curvature stress sensor. This enables its use in the so-called 'multi-layer residual stress depth profiler' (MLSDP), which is currently in development at the Eindhoven University



(a) Schematic overview of the microbalance design with all components, including the control system (PC).

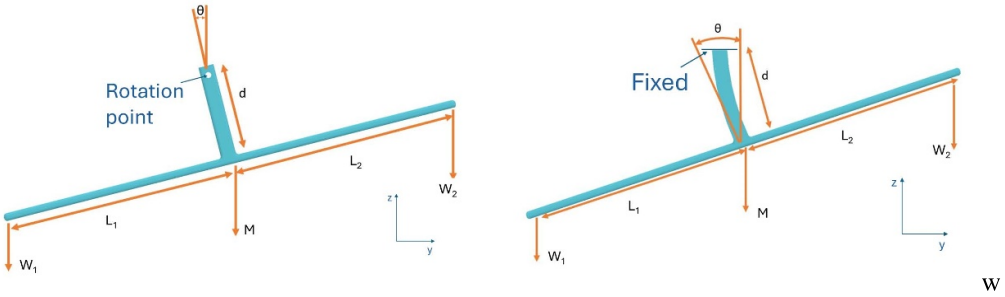


(b) Cross section of the CAD model of the MLSDP without the wafer-curvature stress sensor and PC.

Figure 2. Overview of the microbalance design with all components: 1) Moving part of the microbalance including (a) Fulcrum and (b) Rotating beam; 2) Pins to elevate the sample; 3) (a) Counterweight and (b) Sample; 4) Static part of the microbalance including built-in stops for the moving parts; 5) Undercarriage for installation of capacitive sensors and actuators; 6) Capacitive sensors to measure the deflection; 7) Circular plates for actuator and sensors; 8) Mount to install microbalance to vacuum chamber including Haberland cross spring to facilitate rotation of the balance; 9) Micrometer to rotate the microbalance; 10) Vacuum chamber with multiple viewports for optical access; 11,12) wafer-curvature stress sensor with (11) the Lightsource (LED) and (12) the Optical sensor (CMOS camera); 13) Piezoactuator with strain gauge for calibration; 14) Pushback-mechanism with shutter; 15) Plasma setup for etching; 16) Micrometer with capacitor plate for actuation of the microbalance; (17) Protection plate for the microbalance against plasma exposure.

of Technology in the Netherlands [53]. The MLSDP measures the residual stress as a function of thickness for multilayer stacks on a wafer and consists of three components: (i) a plasma setup that operates in a vacuum to homogeneously etch the material layer by layer, (ii) a stress-curvature sensor to measure the resulting change in residual stress *in situ* [54], and (iii) the here-proposed microbalance to measure the minute weight change which is converted to a thickness change using the density of the removed material. The microbalance, therefore, has been designed to have an unobstructed light path from the stress sensor to the bottom of the sample while ensuring that the sample remains mechanically unconstrained such that it can freely curve [32, 34].

The microbalance consists of diverse components and auxiliary parts, as shown in the schematic overview in figure 2(a) and the cross-sectional view of a CAD model of the MLSDP in figure 2(b). The microbalance features two V-shaped leaf springs acting as a fulcrum (1a), with the design detailed in section 3.1. A rotation beam (1b) is attached to the fulcrum to convert rotation into deflection, as explained in section 3.2. Pins (2) are firmly attached to the rotating beams to lift both the sample (3b) and the counterweight (3a), increasing the sensitivity of the microbalance. To ensure durability, the microbalance is encased in a housing (4) with built-in stops to prevent plastic deformation of the leaf springs. This requires a special manufacturing process, which is described in section 3.4.



(a) Rotating beam connected to a rigid bar, which can freely rotate from the rotation point at the top. A change in moment results in the rotation of the rigid bar, resulting in a rotation of the beam.

(b) Rotating beam connected to a cantilever, of which the rotation and displacement are fixed at the top. A change in moment deforms the cantilever, which causes a rotation of the beam.

Figure 3. Deformation of the microbalance due to a mass difference. W_1 and W_2 are the masses on the left and right sides, θ is the rotation of the beam, and d is the distance from the fixation point of the microbalance to the beam, and M is the mass of the beam.

The deflection of the rotating beam is measured using capacitive sensors (6), which require a minimum surface area to perform a measurement. Therefore, circular plates (7) are glued to the microbalance (section 3.6). The capacitive sensors are installed in an undercarriage (5), and the undercarriage is securely attached to the microbalance. Cooling blocks are attached to the sides of the undercarriage to minimize temperature gradients and are therefore not visible in figure 2(a) but are discussed in section 3.7. The microbalance and undercarriage are mounted in a structure featuring a cross spring and a micrometer (9) for leveling of the microbalance, as explained in section 3.8. This mount is connected to the vacuum chamber (10) via bobbins to minimize vibrations. The vacuum chamber has viewports for measurements with an optical stress sensor (11) captured by a camera (12). The automatic calibration mechanism, which includes a piezo actuator (13) and a pushback mechanism (14), is detailed in section 4.1. This mechanism enables the microbalance to operate in demanding environments, such as during sample deposition or etching. These processes require a stabilization period to ensure that all parameters are stable. During this period, a shutter integrated into the pushback mechanism (14) protects the sample from the plasma (15). For thick layer removal or deposition, the range is extended by keeping the microbalance in its null position using an actuator (16), as discussed in section 5. This actuator only needs to be installed on one side of the microbalance. To enhance the force exerted by the actuator, a circular plate (7) is glued to the microbalance. Another circular plate is added to the opposite side to maintain symmetry.

3. Detailed design

The original beam microbalance concept has the largest load capacity to resolution ratio and is vacuum-compatible [25]. Therefore, the beam microbalance concept has been chosen as the basis for the new microbalance. Conventional beam microbalances, however, have a large footprint to be sufficiently sensitive to weight changes. The larger the rotating beam, the bigger the change in moment. This moment change causes a rotation, resulting in a deflection that increases with beam length. Therefore, to decrease the footprint of the microbalance while keeping the resolution the same, the fulcrum needs to be redesigned to become more sensitive to a change of moment.

3.1. Fulcrum selection

To understand the mechanics of the problem, the fulcrum is initially assumed to be a rigid bar, see figure 3(a), which is able to rotate freely at the top. A change in moment due to a mass difference, evidently, results in a rotation of the microbalance. This rotation shifts the center of gravity, and an equilibrium position is reached in which the moment caused by this shift equals the moment due to the mass difference. This moment balance gives $\theta = \frac{W_1 L_1 - W_2 L_2}{(W_1+W_2+M)d}$, in which L_1 and L_2 are the arm's length at the left and right side, respectively, W_1 and W_2 are the masses on the left and right side, θ is the rotation of the beam, M is the mass of the rotating beam, and d is the length of the rigid bar [25]. In this simple example, the small mass of the rigid bar and the rotational stiffness at the top of the rigid bar is neglected, i.e. it can freely rotate at the top. The mechanics changes if the rigid bar is replaced by a flexible cantilever (e.g. a leaf spring), see figure 3(b). A leaf spring has a moment equal to $k\theta$ in which $k = EI/d$ with E is Young's modulus, I the second moment of inertia, and d the length of the cantilever. Additionally, when a beam rotates, the center of gravity shift (either to the left or right) is only approximately half the magnitude compared to that of a rigid bar. This is because the horizontal deflection measured at the end of the cantilever is half the magnitude at a certain angle compared to a rigid bar [55]. The moment balance then gives $\theta = \frac{W_1 L_1 - W_2 L_2}{(W_1+W_2+M)\frac{d}{2}+k/g}$ in which g is the acceleration due to gravity. Finally, the vertical deflection of the beam is calculated by multiplying the arm length by angle θ. In reality, however, the curvature of the cantilever is non-uniform due to the weight pulling at the cantilever.

From the above calculations, an estimation is made for the dimensions of the leaf spring. However, it is essential to ensure that the microbalance rotations and displacement are fully constrained except for the intended axis of rotation. Using a single

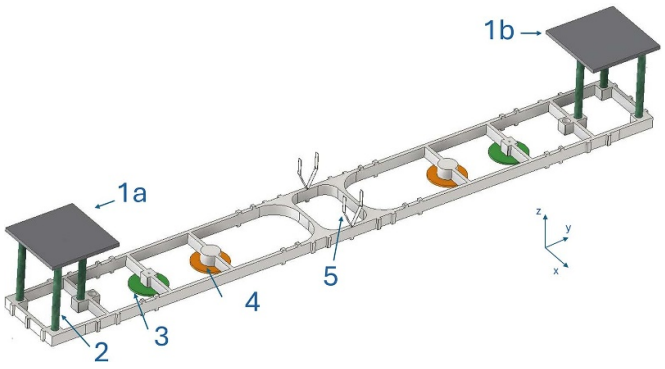


Figure 4. CAD model of the inner part of the microbalance. The sample (1b) and counterweight (1a) are placed on pins (2), which are inserted at the end of the microbalance. The green (3) and orange (4) plates are used by, respectively, the actuator to keep the microbalance in its null position and the capacitive sensors to measure the deflection.

leaf spring does not provide sufficient constraint, allowing unacceptable movements and rotations. To address this issue, four wide leaf springs have been used as a fulcrum, arranged in two pairs of V-shaped configurations. The optimization of the fulcrum is explained in section 3.3.

3.2. Design of the beams

The rotating beam is connected to the leaf springs. The beam design must facilitate optical access to the bottom of the sample while providing sufficient space for beam deflection measurement and microbalance actuation. The sensitivity of the microbalance is determined by the rotational stiffness of the fulcrum and the vertical distance between the center of rotation and the center of gravity [25]. Since the center of gravity of the rotating beam is below the center of rotation, a mass reduction of the rotating beams increases the center of gravity and, therefore, the sensitivity. To reduce the mass of the rotating beam while retaining its structural stiffness, large inner sections have been removed to create a frame of two slender beams connected with struts, see figure 4. The struts connecting the rotating beams support essential components for microbalance actuation and deflection measurement. The struts are positioned approximately 2 cm apart to prevent interference between the deflection measurement and the actuation, thereby ensuring accurate results. Furthermore, to increase the sensitivity, the samples have been elevated by installing three pins at each end of the microbalance, as shown in figure 4. Additionally, elevating the samples above the microbalance provides an opportunity to enclose the microbeam in a protective housing, which is the monolithic block from which the microbalance is manufactured, as discussed below.

3.3. Optimization of the microbalance

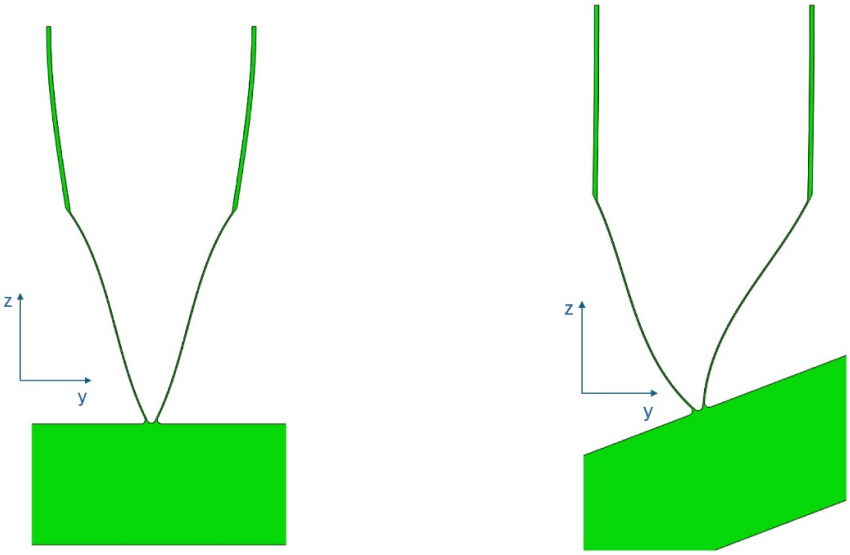
The complete microbalance has been modeled with FEM using quadratic tetrahedral solid elements to perform a structural and thermal analysis; see figure 5. The leaf springs have been optimized in shape and dimensions to reveal the highest sensitivity while being robust to all possible unwanted deformation modes. The result is that each of the four leaf springs has a lower 30 μm thick leaf spring with a length of 5 mm under an angle of 30°, resulting in a remarkably low rotational stiffness and, therefore, a very sensitive fulcrum. The lower part of the leaf spring is connected to the fixed base via an upper thicker 200 μm thick leaf spring under 0° angle, see figure C.2(b). Plastic deformation of the lower leaf springs due to overloading of the microbalance is prevented by the deformation of the upper leaf springs against built-in stops. To constrain all degrees of freedom except the rotation around the y-axis, the leaf springs are designed with a 1 mm width and arranged in pairs, forming a double V-shape. These V-shaped leaf spring pairs are positioned 18 mm apart in the y-direction for maximum robustness.

The rotating beams have also been optimized for performance, robustness, and manufacturability. Any mass above the rotational point increases the sensitivity, while mass below the rotational point decreases the sensitivity [25]. The rotating beam is located below the rotational point and should, therefore, be very light for maximum sensitivity. In the current design, the beam has been chosen to be as light as possible while preserving the manufacturability and good thermal properties. The rotating beams have a total length of 18 cm, a height of 3 mm, and a width of 1 mm. The two slender side beams and connecting struts have a width of 1 mm, see figure C.2(a).

For the final microbalance design, the sensitivity is determined for different load conditions. For samples of 1 g, a sensitivity is found of 36.8 nm μg^{-1}, and for samples with almost zero mass, the sensitivity is 27.3 nm μg^{-1}. Furthermore, the behavior when the microbalance is not leveled in the mount has been simulated, and the resulting error for rotations of the base of the microbalance below 1° is below 0.1 nm μg^{-1}. Note that the resulting change in sensitivity would be detected by calibrating the microbalance.

3.4. Manufacturing of the microbalance

The leaf springs are extremely fragile since they are only 30 μm thick, as measured using scanning electron microscopy, see the SEM images in figure A.2. Using additive methods would have caused the leaf spring to fail during manufacturing, as the process induces stresses exceeding the yield stress. Here, the microbalance is made by only removing material from a solid bar of Ti-6Al-4 V (tensile yield strength 880 MPa, compressive yield strength 970 MPa, Young's Modulus 113.8 GPa), chosen for its excellent manufacturability and large yield strain, ensuring the elastic behavior of the microbalance [56, 57]. Moreover, the balance is then a single monolithic piece, see figure 6. To prevent potential residual stresses, a stress-relieve heat treatment is applied before starting the Electric Discharge Machining (EDM) procedure, explained below, which explains the discoloration in figure 6(b). To produce the microbalance, the design incorporates multiple fixation points for manufacturing, see figure 7(a), preventing



(a) The deformed leaf springs are pulled inwards due to the weight of the microbalance. Deformation scale factor = 100.

(b) The left-side sample is 100 µg heavier, causing a microbalance rotation and deforming both lower parts of the leaf springs into an S-shape. Deformation scale factor = 500.

Figure 5. Finite element method (FEM) analysis of microbalance. The microbalance is discretized with quadratic tetrahedral elements with local mesh refinement. Deformations of the microbalance due to its own weight or weight difference between the left and right side are minute, therefore, after running the simulation, a deformation scale factor of respectively, (a) 100 and (b) 500 have been applied to make the deformation visible.

the microbalance from moving during production. These fixation points are subsequently removed after manufacturing. Using this manufacturing method, the balance is created inside a single bar, which serves as the housing protecting the microbalance. This manufacturing method also makes it possible to incorporate built-in stops to prevent plastic deformation of the microbalance, as discussed in section 3.5.

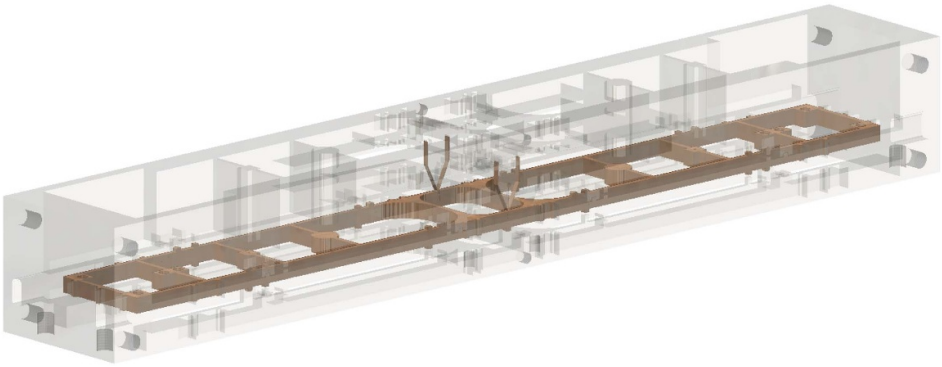
Two methods are used to remove material. First, EDM removes material with a positioning accuracy of 5 μm, whereby the wire needs to pass through the block of material from one side to the other in a straight line [58, 59]. Second, micromilling enables material removal without the need to traverse through the material completely but is only suitable for sections where the manufacturing precision is less restrictive. Micromilling also causes vibrations, which might damage the microbalance if delicate structures are already present and should, therefore, be done prior to EDM. Therefore, the microbalance is manufactured by first performing micromilling on all six sides of the heat-treated bar of Ti-6Al-4 V, see figure C.1 for the bar of Ti-6Al-4 V after micro-milling. The bar is heat treated again, and EDM is used on two sides to finalize the microbalance, including manufacturing of the leaf springs and built-in stops, after which the fixation points are removed, see figure 7 with close-up photographs of the leaf springs shown in figure C.3.

After using EDM and micromilling, specially designed sample supporting pins, limiting any clearances, are installed vertically to elevate the sample, three on each edge of the rotating beam, as shown schematically in figure 4. Ruby balls, minimizing friction, are attached at the top of the pins, as shown in detail in figure 9(a) below, onto which the samples are placed.

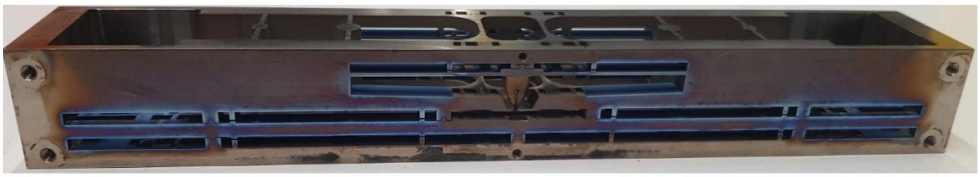
3.5. Built-in stops

Thinner leaf springs result in a more sensitive microbalance. However, a thinner leaf spring has a higher maximum tensile stress for the same sample weight and, therefore, tends to deform plastically earlier [55]. In existing designs of springs, cantilevers, and beam microbalances, a compromise had to be made between robustness and sensitivity [23, 25]. In our design, this limitation has been largely circumvented by constraining the range of motion of the microbalance. Built-in stops prevent overloading of the microbalance in all directions for all deformation modes, see figure 7. As a consequence, the microbalance can be flipped upside down without problems to allow for repairs or overloaded with heavy sample (tested up to $>$30 g). The built-in stops limit the range of motion of the rotating beam to approximately 170 μm and the leaf springs to approximately 200 μm. More detailed views of the microbalance and the internal built-in stops are shown in figures C.4 and C.5.

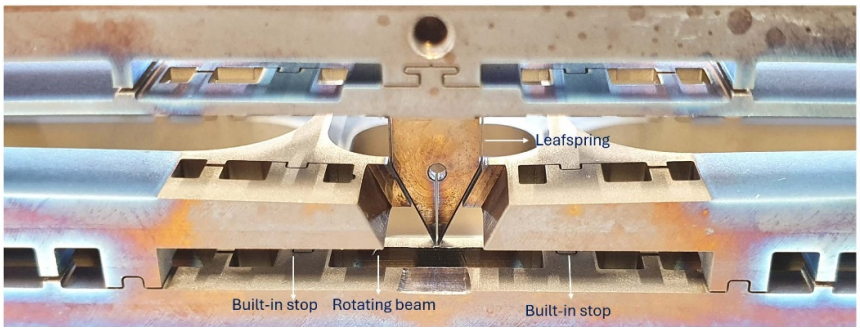
If the range of motion would not be limited, the microbalance would immediately fail during manufacturing, and it would not help to install the built-in stops afterward. To prevent this, the built-in stops are part of the design and manufacturing procedure. As discussed in the previous section, the EDM procedure removes material, monolithically shaping the microbalance with the built-in stops integrated. The support points, see figure 7, which are removed after completion by EDM, hold the microbalance in place during manufacturing and ensure a well-defined position and size of the built-in stops. These stops precisely limit the range of motion of the microbalance.



(a) CAD model of the microbalance, with transparent monolithic housing to show the moving part of the microbalance, i.e. the V-shaped leaf springs and rotating beam (colored brown), inside the protective housing.

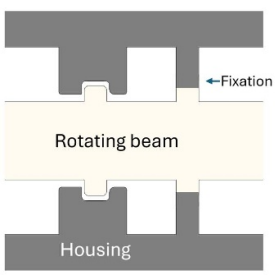


(b) Front view photograph of the manufactured microbalance.

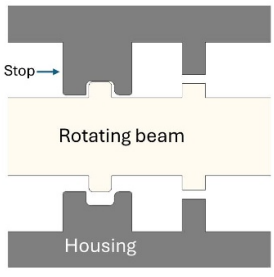


(c) Close-up photograph of the V-shaped leaf springs of the microbalance.

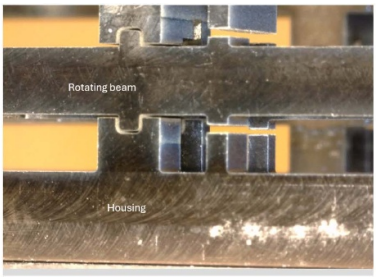
Figure 6. CAD models and pictures of the microbalance.



(a) Schematic representation of (left) the built-in stops and (right) the fixation points that are permanently removed before operation, see subfigure (b) and (c).

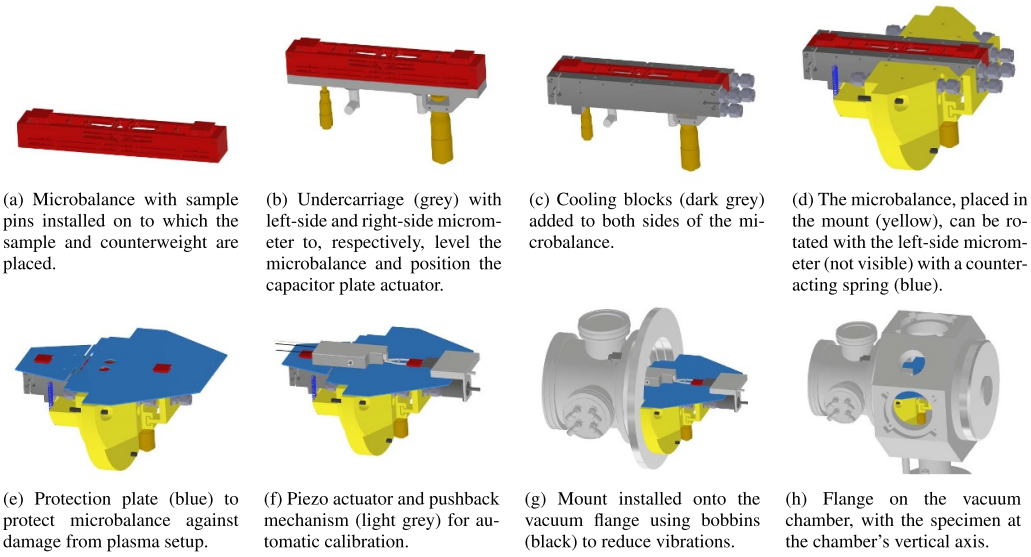


(b) The microbalance shown under an overload condition, causing the rotating beam to contact the built-in stop that prevents damage.



(c) Photograph of one of the microbalance's several built-in stops and fixation points; the built-in stop constrains the vertical motion of the rotating beam.

Figure 7. Fixation points and built-in stops to prevent plastic deformation during, respectively, manufacturing and normal operation.



(a) Microbalance with sample pins installed on to which the sample and counterweight are placed.

(b) Undercarriage (grey) with left-side and right-side micrometer to, respectively, level the microbalance and position the capacitor plate actuator.

(c) Cooling blocks (dark grey) added to both sides of the microbalance.

(d) The microbalance, placed in the mount (yellow), can be rotated with the left-side micrometer (not visible) with a counteracting spring (blue).

(e) Protection plate (blue) to protect microbalance against damage from plasma setup.

(f) Piezo actuator and pushback mechanism (light grey) for automatic calibration.

(g) Mount installed onto the vacuum flange using bobbins (black) to reduce vibrations.

(h) Flange on the vacuum chamber, with the specimen at the chamber's vertical axis.

Figure 8. Assembly of the microbalance with auxiliary parts in the vacuum chamber.

3.6. Deflection measurements

The deflection of the rotating beams due to the rotation at the fulcrum is measured with two capacitive sensors. The capacitive sensors employed here (Micro-Epsilon Capacitive displacement sensor CSE1,25/M12 together with a demodulator with integrated preamplifier DL6220) operate at low voltage, minimizing the applied force to the microbalance to below 10^{-8} N [60]. The sensors have a resolution of 0.9 nm at 2 Hz and a resolution of 25 nm at 8.5 kHz but need a minimum surface area to measure the distance [61]. Therefore, lightweight copper plates are glued underneath the rotating beam. The best position for the deflection measurements is located at the end of the beams since the deflection has its maximum value there. However, the stress sensor needs to be able to measure the curvature from below, so the capacitive sensors would obstruct the stress sensor in measuring the curvature of the sample. Secondly, other devices that benefit more from being positioned at the beam's end are installed there, enhancing the microbalance's specifications, see sections 4 and 5. Moreover, the capacitive sensors exert a small force on the microbalance, which results in a smaller change of moment when positioned closer to the center of rotation. Accordingly, the capacitive sensors are positioned closer to the center, see figure 4. An undercarriage has been designed to install the capacitive sensors. The undercarriage is firmly attached underneath the microbalance, see figure 9(b). The undercarriage also features a slot for a micrometer to position the actuator, which is explained in section 5.

3.7. Minimizing detrimental effects of plasma setup

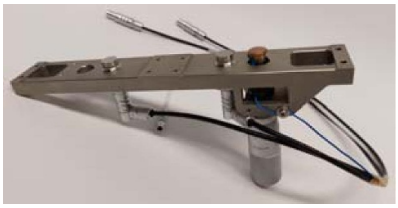
The microbalance is used with a plasma setup to remove material from the sample, placing it in a challenging operational environment. During normal experiments, the plasma setup only removes material from the sample location, however, while fine-tuning the plasma setup, the plasma might damage the microbalance [62–64]. Therefore, a protection plate is installed above the microbalance, see figure 8(e). It also takes some time for the plasma to stabilize after initiation. The experiments only start after the plasma setup has stabilized. Therefore, a shutter is installed to cover the sample to prevent material from being removed before the setup is stable, as detailed in figure 13(a) below. The plasma setup also locally heats the microbalance. The design and choice of material for the rotating beams and sample pins help to mitigate the effects of heating. Additionally, cooling blocks are installed on both sides of the microbalance block to minimize temperature gradients. Water is recirculated through these blocks to redistribute and evacuate the heat, see figure 9(c).

3.8. Monolithic mount for the microbalance in the vacuum system

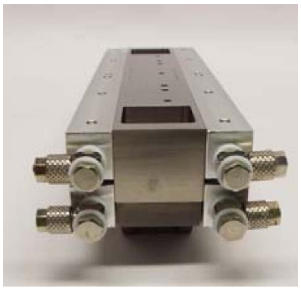
A monolithic mount mechanism has been designed to install the micro-balance with the cooling, protection plates, undercarriage, and shutter into a vacuum chamber, see figure 8 for the complete assembly and figure 10 for the mount. Rubber bobbins connect the mount with the vacuum chamber and damp vibrations, see figure 8(g). Cooling channels are drilled through the mount and connected at one side to the cooling blocks and at the other side to a pump located outside the vacuum. The micro-balance with the cooling and undercarriage is installed in the mount mechanism. The microbalance is supported on one side by the right-side micrometer head and on the other side by the beam between the Haberland cross-spring hinge. The micrometer head makes it possible to rotate the microbalance to level it. The Haberland cross-spring hinge on the other side has a built-in stop to limit the range of rotation, see figure 10(c). Finally, note that all the CAD drawings are available to the reader by request to the authors to facilitate easy reproduction.



(a) The three sample pins with ruby balls at their top onto which the sample is placed.

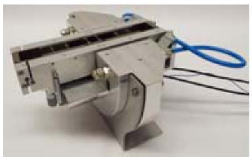


(b) Microbalance undercarriage with the two capacitive sensors with black cables and the right-side micrometer to position the capacitor plate actuator with blue cable

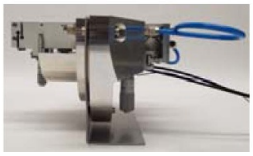


(c) Cooling blocks on both sides of the microbalance in which water flows through internal channels.

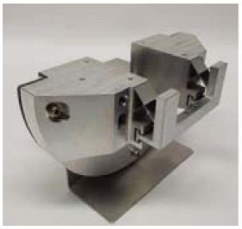
Figure 9. Close-up photos of different components of the microbalance.



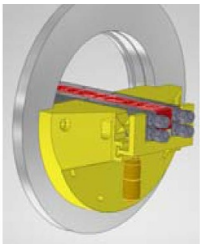
(a) A special holder securely positions the mount with microbalance outside the vacuum chamber.



(b) The mount from a different angle, with both micrometers visible.



(c) The Haberland cross spring pivot, with stops, to enable rotation of the microbalance.



(d) CAD drawing of the mount installed on the vacuum flange.

Figure 10. Photographs of the mount with which the microbalance is installed in the vacuum chamber, including cooling channels and a mechanism to level the microbalance.

4. Calibration

As shown above, the sensitivity of the microbalance has been determined with FEA. The experimental sensitivity may vary due to minor deviations in the actual dimensions of the leaf spring and the use of the microbalance in different environments. Therefore, proper calibration of the microbalance remains essential for accurate operation during, e.g. deposition and etching processes.

First, a manual calibration has been performed at atmospheric pressure with calibrated weights up to 500 μg. The weights are carefully placed on the microbalance, and the deflection has been measured at the capacitive sensors, see figure C.6. The sensitivity of the microbalance experimentally determined by both sensors is 76.2 nm μg^{-1} and 75.9 nm μg^{-1}, respectively, see figure 11. This sensitivity is approximately twice as high as numerically predicted and is caused by a number of reasons: the leaf springs are a few micrometers thinner than designed, the beam is a bit lighter than expected, and the microbalance has a higher center of gravity than calculated due to the longer vertical sample supporting pins used when the ruby balls are glued at the top of the pins. These ruby balls are above the rotational point, increasing the sensitivity. Given the capacitive sensor's manufacturer-specified resolution of 25 nm at a sampling rate of 8.5 kHz, the microbalance should achieve a single-measurement point resolution below 0.3 μg. In our application, many measurements

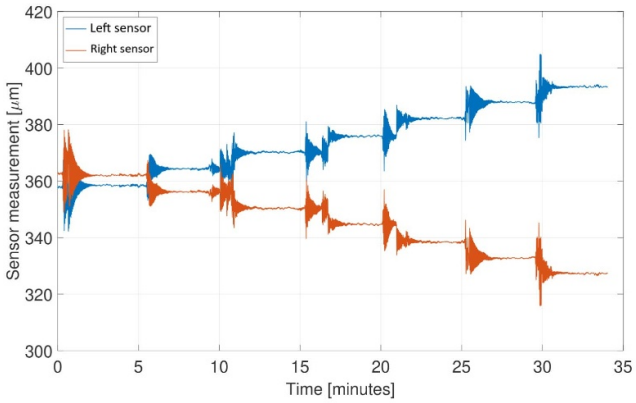
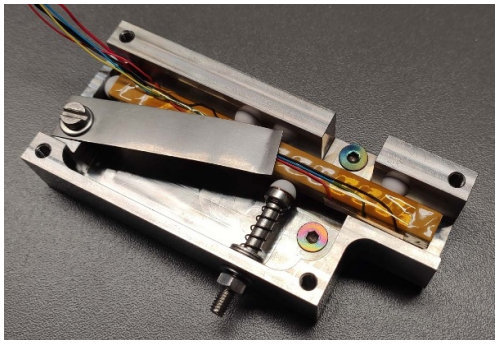
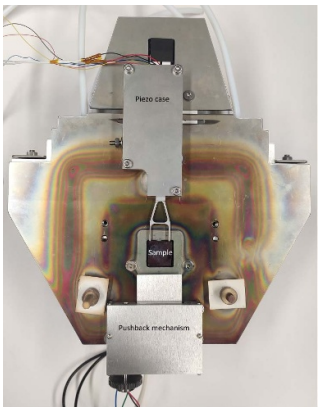


Figure 11. Manual calibration of the microbalance. The experiment is conducted at atmospheric pressure due to the manual placement of the weight on the microbalance. This process initially causes significant vibrations, which damp out over time. The deflection is obtained by determining the equilibrium position after the vibrations are damped. The identified sensitivity for the capacitive sensor on the right and left side are, respectively, 75.9 ± 0.2 nm μg^{-1} and 76.2 ± 0.2 nm μg^{-1}.

are performed at a lower frequency of 100 Hz, and the measurements are always averaged over time, resulting in a resolution that is well below 0.1 μg, which explains why the values of 76.2 nm μg^{-1} and 75.9 nm μg^{-1} are so close.



(a) The case holding the piezo actuator and constraining all its DOFs except one, allowing motion in one direction only. The rigid fork extension is glued to the piezo actuator end (not shown).



(b) Topview of the piezo actuator installed on the microbalance, with the piezo-actuator case and pushback mechanism indicated.

Figure 12. The automated calibration setup with (a) the piezo actuator in its invar casing and (b) the piezo actuator and pushback mechanism installed on the setup, with the rigid fork extension of the piezo actuator displacing the specimen without rotation.

4.1. Automic calibration

The plasma setup affects the microbalance's sensitivity, making calibration in vacuum conditions crucial. To facilitate this, an automatic calibration mechanism has been developed. Typically, a weight variation leads to a moment alteration, which the fulcrum transforms into rotation, causing a deflection captured by the capacitive sensors. In the automated calibration setup (ACS), the weight remains unchanged, but the arm length of the sample is altered, changing the moment. The ACS thus determines the balance's sensitivity to moment changes, which is then converted to a weight change sensitivity using the arm's length and the (externally measured) sample weight.

The ACS is shown in figure 12, with a side view photograph shown in figure C.7 . A piezo actuator on the left side of the sample moves the sample, changing the arm length of the sample in a controlled manner. The sample is positioned on the sample pins. Due to friction between the sample and the pins, the pins could deflect slightly. To prevent this, the pins are designed sufficiently stiff to have a deflection below the accuracy of the piezo actuator [65]. The piezo actuator, equipped with a strain gauge, is mounted in a way that constrains all degrees of freedom except the one needed to displace the sample. Since the piezo actuator can only push and not pull, a pushback mechanism with stepper motor is placed on the other side to move the sample opposite the piezo actuator's motion, see figure 13. To prevent the stepper motor from exerting an excessive force, it drives a spindle attached to a leaf spring mechanism, which gently pushes the sample back to the piezo actuator, see figure 13(b). This pushback mechanism also includes the shutter, see figure 13(a), with a photograph of the plasma cover of the pushback mechanism shown in figure C.8.

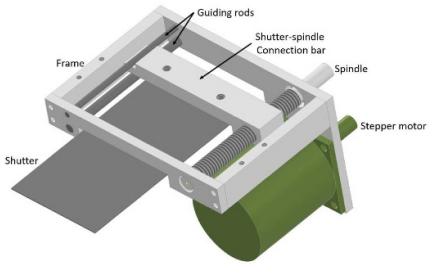
To start the calibration process, the piezo actuator is moved to its initial position. The pushback mechanism, driven by the stepper motor, pushes the sample against the piezo actuator and then retracts. The piezo actuator extends slowly in 10 μm steps to push the sample, preventing overshooting. After each extension, the piezo actuator is temporarily retracted, and the deflection change is measured. The experiment stops at 100 μm. With the sample's weight and change in arm length precisely known, the sensitivity to a change in arm's length is converted into weight change sensitivity.

Figure 14 shows the calibration results. The x-axis represents the change in arm length converted to a weight change, while the y-axis shows the microbalance deflection measured by the capacitive sensor. The slope gives a sensitivity of 79.4 ± 0.2 nm μg^{-1}. The results also indicate that the sensitivity is independent of the applied weight, demonstrating that the microbalance behaves linearly. This linearity simplifies the measurement process across a broad range of weights.

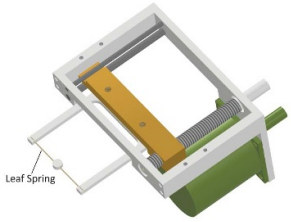
5. Extended weight range

The manufactured distance between the built-in stops is 170 μm, which limits the range of the microbalance. With a sensitivity of 79.4 ± 0.2 nm μg^{-1}, the maximum weight difference it can measure is 2.1 mg, meeting the set requirements (set originally for multilayer stress depth profiler developed at the Eindhoven University of Technology).

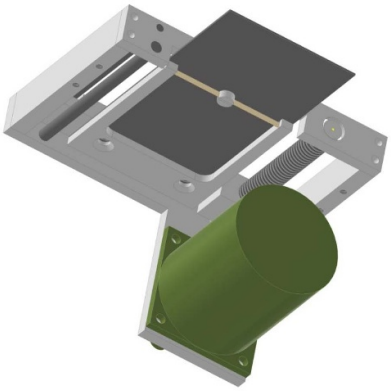
To enhance the microbalance for general use, its range needs to be increased. This can be achieved by applying a force to maintain the microbalance in its null position [43], making the range dependent on the applied force rather than the built-in stops. This force is linearly related to the weight change. To increase the range, a force up to 3×10^{-5} N with an accuracy of 10^{-8} N needs to be applied. A common way is to apply a magnetic force by placing a magnet inside a coil [66, 67]. By means of detailed 3D magnetic field calculations (not shown), it is found that a single silicon iron crystal with a diameter of 0.4 mm and a length of 2 cm should be magnetized in the axial direction to achieve the required accuracy and stability. However, manufacturing these small magnets requires highly



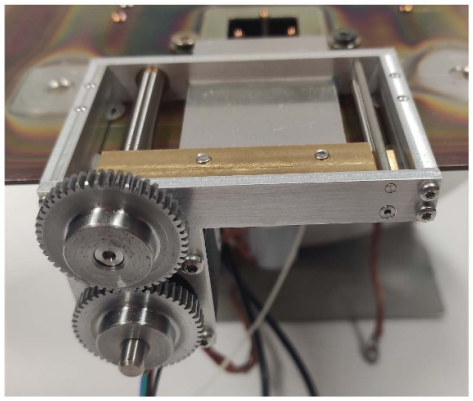
(a) Pushback mechanism with shutter installed.



(b) The leaf spring that pushes against the sample.



(c) Pushback mechanism as viewed from below.



(d) Pushback mechanism installed in the vacuum chamber.

Figure 13. CAD drawings and photographs of the pushback mechanism. Since the piezo actuator can only move the sample to the right, a pushback mechanism is used to move the sample back to the left. The piezo actuator performs the calibration, so the pushback mechanism does not need high accuracy. A flexible leaf spring is installed to prevent the pushback mechanism from applying excessive force.

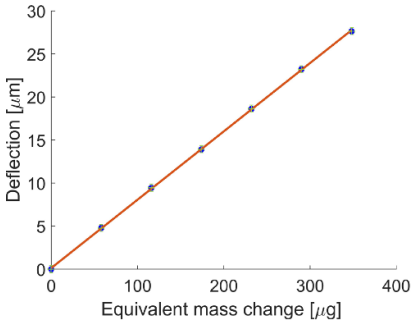


Figure 14. Results of automated calibration of the microbalance. The sensitivity is determined from the slope of the graph and has a value of 79.4 ± 0.2 nm μg^{-1}. Note that the (small) error bars are shown in green.

specialized equipment and skills [68], which were unavailable in this project. The manufactured magnets would also be fragile, so a more robust method is chosen to apply the force.

In our setup, we opt to apply a large force with high precision by utilizing two plates with opposite charges to generate an electrostatic force [69]. The force depends on the voltage between the plates, the distance between the plates, the size of the plates, and the permittivity of the medium in between the plates. One plate is glued to the microbalance, and the other is placed on top of a micrometer head in the undercarriage underneath the other plate, see figures 8 and 9(b). The distance between the plates is set once. Since the force depends on the distance between the plates and the microbalance is moving, the force is non-linear. To control the microbalance to its null position, the offset of the microbalance is measured with the capacitive sensors, and a non-linear control system (in LabVIEW) processes the data from the capacitive sensors and determines the voltage needed to move the microbalance to its null position. The output is sent to a commercial Multifunction Input/Output Device (National Instruments USB-6211) with an update rate of 250k samples per second, a 10 V output range, and an accuracy at a full scale of 3.5 mV. The output is subsequently sent to a non-inverting amplifier with precision op-amps to yield a 50 V output range with an accuracy of 17.5 mV at a maximum output rate of 250k samples per second, outperforming most commercial digital power supplies. The output is measured by a digital multimeter with an accuracy of 4.1 mV and fed into the non-linear control system to correct the output, see figure C.9 for a schematic overview of the system. After applying a constant average window equal to the period of the vibrations, a precision is obtained of 2×10^{-8} N. This means that the maximum weight difference is extended to at least 10 mg, while the accuracy of the microbalance is not compromised.

6. Discussion

The microbalance has been designed to be insensitive to uniform temperature changes. However, localized heating from the plasma setup can cause temperature imbalances. To mitigate this, the rotating beam's heat conductivity is

maximized and radiation minimized by using a material with high thermal conductivity and low emissivity (Ti-6Al-4 V), and by designing the rotating beam with a large cross-sectional area. This promotes a uniform temperature distribution across the rotating beam. The sample support pins are optimized to dissipate heat to the environment rather than conduct it to the rotating beam by maximizing radiation and minimizing thermal conductivity. This is achieved by using thin, long pins made of a material with low thermal conductivity (aluminum) and coated with a high emissivity layer [25]. Additionally, a shutter protects the sample during the stabilization of the plasma setup, allowing the system to reach a stable temperature before the weight measurement begins. Another potential approach involves integrating capacitive sensors into the housing to measure beam expansion due to temperature fluctuations, which could expedite the measurement process, however, this method has not yet been tested.

Temperature gradients cause Knudsen forces, which are also pressure-dependent [70]. At pressures below 10^{-3} mbar and above 1 mbar, Knudsen forces are minimal [71]. However, within this range, the Knudsen forces can reach values around 10^{-6} N. If these forces acted equally on both sides of the microbalance, it would not affect the measurements. However, the temperature gradient is higher on the side of the plasma setup, resulting in a higher Knudsen force on that side. By heating the side where the counterweight is placed and cooling the side where the plasma is activated, the temperature gradients are minimized, thus reducing potential Knudsen force effects.

The microbalance can be further improved by extending its maximum weight difference range. While the control system offers one method for range extension, another effective approach involves adjusting the arm length of the sample on either side. For deposition processes, if the microbalance hits the lower stop on the right side, the sample on the right can be moved inward with the pushback mechanism (with ACS removed), where a movement of 200 μm corresponds to an additional 2 mg measurement range, and this process can be repeated until a movement of a few millimeter before the specimen falls off the pins, extending the range with tens of milligrams. Alternatively, a stepper motor with a leaf spring, similar to the pushback mechanism, can be installed next to the counterweight on the left for either etching or deposition processes, with the advantage that the ACS of in-situ calibration does not have to be removed. Note that after each sample or counterweight movement, the microbalance sensitivity constant needs to be adapted based on the presumed applied sample displacement. With the ACS in place, however, the automatic calibration system can be used to recalibrate the balance *in situ* after each sample movement.

7. Conclusions

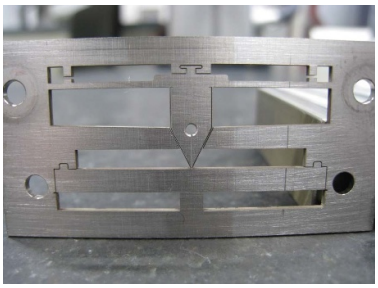
The ongoing miniaturization of electronic devices relies on stacks of thin films with decreasing dimensions. To understand the manufacturing process of these devices and increase their lifetime and performance, it is important to monitor their mass change during various physical processes involved in manufacturing, including material addition or removal during physico-chemical reactions and thin-film micro-fabrication. Despite the availability of various microbalances, none fully met the requirements. To address this, a novel monolithic beam microbalance has been developed from a single block of Ti-6Al-4 V using a dedicated manufacturing process involving only electrical discharge machining (EDM) and micromilling. The microbalance features V-shaped leaf springs optimized with finite element analyses for enhanced sensitivity and built-in stops for robustness. The microbalance is vacuum-compatible with a small footprint and has cooling blocks to minimize temperature gradients. An automatic calibration system has been designed to calibrate the microbalance in vacuum or other challenging environments. This has resulted in a microbalance with a demonstrated resolution well below 0.1 μg with a load capacity exceeding 2 g per sample. The built-in stops prevent damage to the microbalance but limit the range of weight variations to 2.1 mg. However, this range has been extended by a control system that maintains the microbalance in its null position. The new microbalance design is capable of monitoring mass changes during complex vacuum processes, such as deposition and etching. The microbalance stands out for its unique combination of high accuracy ($<1\mu$g), high sensitivity ($<0.1\mu$g), large load capacity (>1 g), a compact footprint ($\approx 30 \times 30 \times 10$ cm^3), vacuum compatibility and compatibility with depth profile analyses, and high robustness (capable of handling upside-down repairs and overloading by heavy samples up to $\approx$30 g) provided by integrated mechanical stops. This offers a combination of capabilities not found in existing microbalances.

Data availability statement

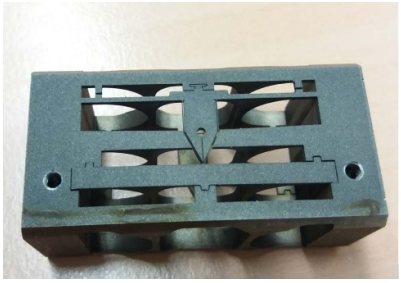
All data that support the findings of this study are included within the article (and any supplementary files).

Acknowledgment

We would like to thank the students Yannick Kieskamp for working on the calibration part and Bram Creusen for designing and installing many parts needed to get the microbalance working. We are also grateful to the Equipment and Prototype Center (EPC) at TU/e for manufacturing the setup and Lucien Cleven for manufacturing the auxiliary parts. This project is partly funded by Position II within the Electronic Components and Systems for European Leadership Joint Undertaking (ECSEL JU) in collaboration with the European Union's H2020 Framework Programme (H2020/2014-2020) and National Authorities, under Grant Agreement Ecsel-783132-Position-II-2017-IA.

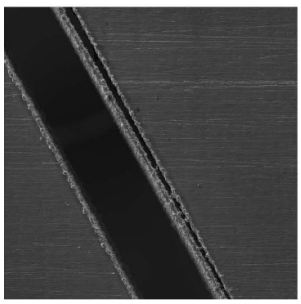


(a) A thin plate to test the settings of the EDM machine. Manufacturing these plates is less time-consuming than manufacturing the whole microbalance and, therefore, is ideal for the initial tuning of the settings.

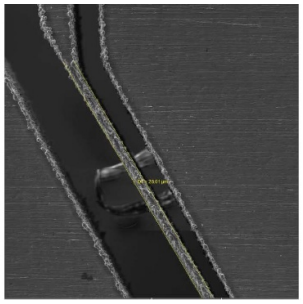


(b) A small part of the complete microbalance to fine-tune the manufacturing settings. After the optimization of this part, the manufacturing of the whole microbalance was started.

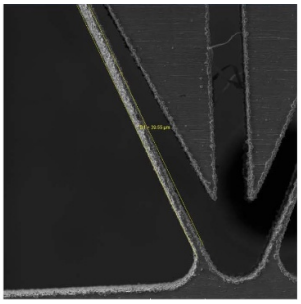
Figure A.1. Testing the manufacturing settings for EDM to obtain a leaf spring with a thickness of 30 μm with minimal deformation of the leaf spring due to residual stresses in the material.



(a) Image of a leaf spring in which the manufacturing settings were incorrect, causing a residual stress that deforms the leaf spring.



(b) Scanning Electrode Microscope (SEM) image of the upper section of the thin part of the leaf spring. The leaf spring has a thickness of around 28 µm.



(c) SEM image of the lower part of the thin part of the leaf spring. The leaf spring has a thickness of around 40 µm.

Figure A.2. Scanning Electrode Microscope (SEM) image of leaf springs manufactured with different settings. The settings that produce a leaf spring with a thickness of $\approx$ 30 μm and minimal residual stress are used to manufacture the complete microbalance.

Appendix A. Manufacturing of the leaf springs

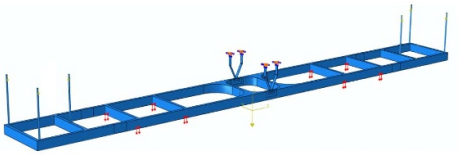
In the microbalance design, leaf springs of 30 μm thick should be manufactured with EDM that are essentially free from residual stress. Manufacturing these leaf springs requires knowledge of the EDM process parameters to obtain the correct dimensions and minimize residual stresses. Ti-6Al-4 V has been chosen as the material for the microbalance because of its high yield strength and available knowledge to process Ti-6Al-4 V with EDM [56, 57]. The sequence in which the material is removed affects the processing results. To test the different settings, the leaf springs are first manufactured in a plate, see figure A.1(a). Since a 2D plate deviates from the microbalance, the manufacturing settings for the microbalance are different. Therefore, before manufacturing the complete microbalance, a 3D cutout of the microbalance has been made, see figure A.1(b). The processing parameters found for this 3D cutout are used for the microbalance. The 3D cutouts are analyzed with a scanning electrode microscope (SEM), see figure A.2. All the four leaf springs must have the same dimensions. However, if they all deviate with the same amount from the designed dimensions, it is less important since the rotational stiffness of the microbalance is calibrated. Residual stresses in the material affects the dynamics of the microbalance and should, therefore, be minimized [72]. As shown in figure A.2(a), residual stresses deform the leaf springs, limiting the range of motion. The settings in which the four leaf springs have the same dimensions and the residual stress is minimal are selected for the final manufacturing of the the microbalance.

Appendix B. Finite element analyses

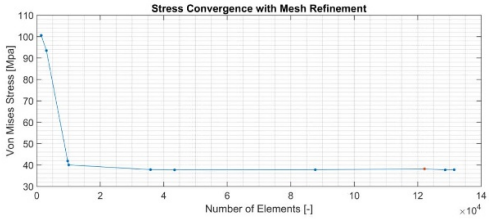
The microbalance is optimized using FEA. The discretization used for this analysis is shown in figure B.1(a). Figure B.1(b) illustrates the boundary conditions and applied loads. A mesh refinement study has been conducted to determine the optimal number of elements for analyzing the micro-balances. Using the applied boundary conditions and forces shown in figure B.1(b), the mesh size was gradually reduced until stress convergence was achieved, as shown in figure B.1(c).



(a) Mesh of the microbalance without the sample pins.



(b) Visualisation of the microbalance with its applied loads and boundary conditions. The tops of the leaf springs are fully fixed. Gravity, represented by the large yellow arrow pointing in the negative Z direction at the center, acts on the entire body. Smaller yellow arrows indicate the weight of the copper plates. Red arrows at each end represent the weight of each sample.



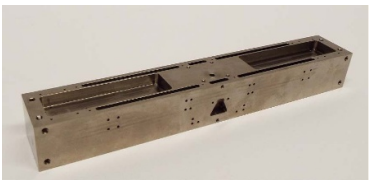
(c) Relationship between the maximum von-Mises stress in the microbalance and the total number of elements in the mesh. The red dot marks the specific number of elements used for the analyses.

Figure B.1. Finite element analysis of the microbalance.

Appendix C. Additional photographs and views of the microbalance

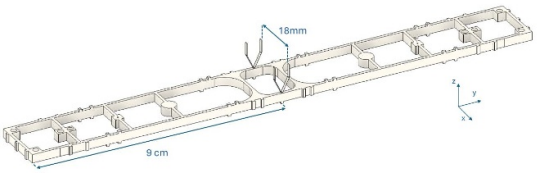


(a) Top view of bar.

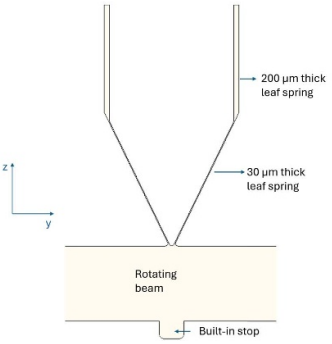


(b) Bottom view of bar

Figure C.1. (a) Bar of Ti-6Al-4 V after micro milling prior to EDM from the top and from the side. The small circular holes in the bar are starting points for EDM. Micromilling is used for removing material at places where EDM is not possible since, with EDM, the wire needs to go completely through the material. Before and after micro-milling, the bar is annealed to reduce residual stresses in the bar. (b) The same bar, viewed from the bottom, after EDM from the top, but before EDM from the side.

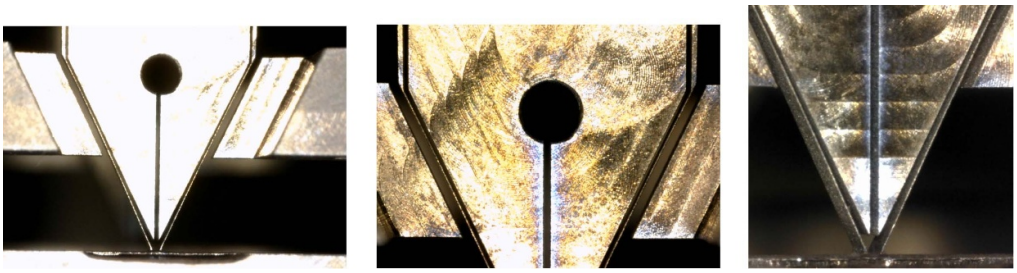


(a) The inner part of the microbalance, showing the leaf springs and the rotating beam that is a frame of two slender beams connected with struts to keep it as light as possible. This part is inside the housing and is solely created by removing material from the bar of Ti-6Al-4V.



(b) Zoom of the leaf springs, the upper part of which has a thickness of 200 µm and the bottom part a thickness of 30 µm. The protrusion at the bottom is used for the built-in stop.

Figure C.2. CAD models of the inner part of the microbalance.

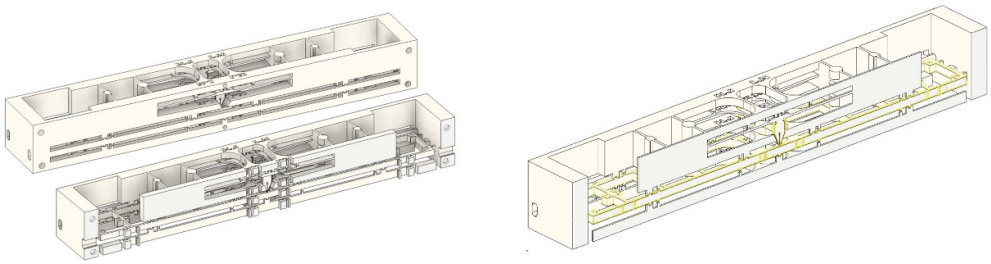


(a) The leaf springs are protected against plastic deformation by the solid structure inside the leaf springs.

(b) The purpose of the hole in the middle is to serve as a starting point for EDM.

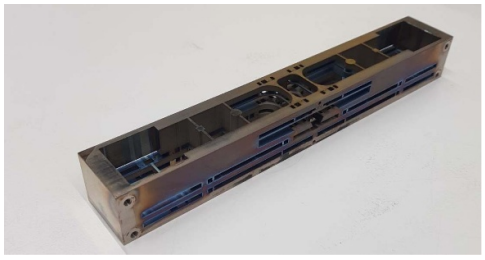
(c) The attachment of the leaf-springs to the beam of the microbalance.

Figure C.3. Zoom-in on the leaf springs in the microbalance.



(a) CAD model of (above) the microbalance housing and (below) a cross-sectional view exposing the inner part and with many built-in stops to protect the microbalance against plastic deformation.

(b) Different cross-sectional view of the microbalance. The leaf springs and rotating beams are highlighted in yellow.



(c) Another view of the microbalance.

Figure C.4. CAD models and pictures of the microbalance. By removing material from the bar of Ti-6Al-4 V, the microbalance is manufactured in a single piece containing the protective housing.

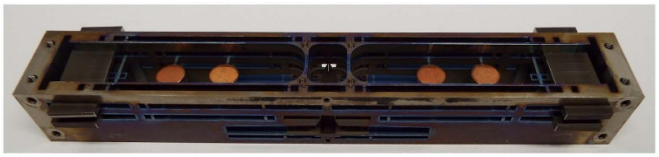
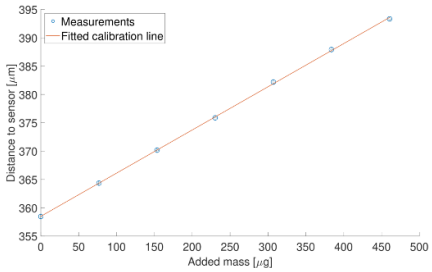
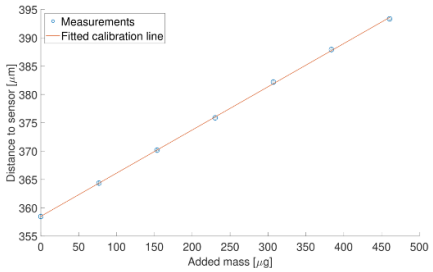


Figure C.5. Microbalance turned upside down to show the plates glued at the bottom of a microbalance. The two inner plates are for the capacitive sensors to measure the deflection, and the outer plates are for the actuators to keep the microbalance in its null position.



(a) Results from the capacitive sensor on the right side. The slope of the graph gives the sensitivity of the microbalance: 75.9 ±0.2 nm/µg.



(b) The weights are placed on the right side of the microbalance. Therefore, the microbalance moves upwards on the left side of the microbalance. A sensitivity is found of 76.2 ±0.2 nm/µg.

Figure C.6. Results of the manual calibration of the microbalance as shown in figure 11. Note that the error bars are approximately the size of the dots.

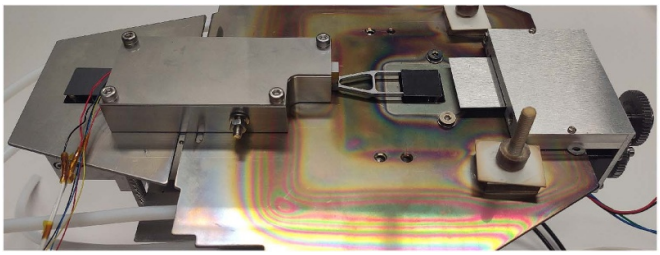


Figure C.7. Side view of the piezo actuator (left) and the pushback mechanism (right).

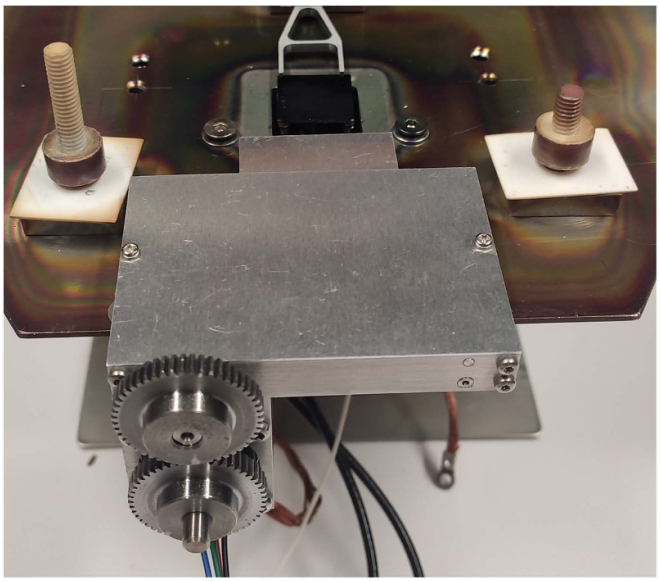


Figure C.8. Pushback mechanism with an additional cover installed to protect it from the plasma setup.

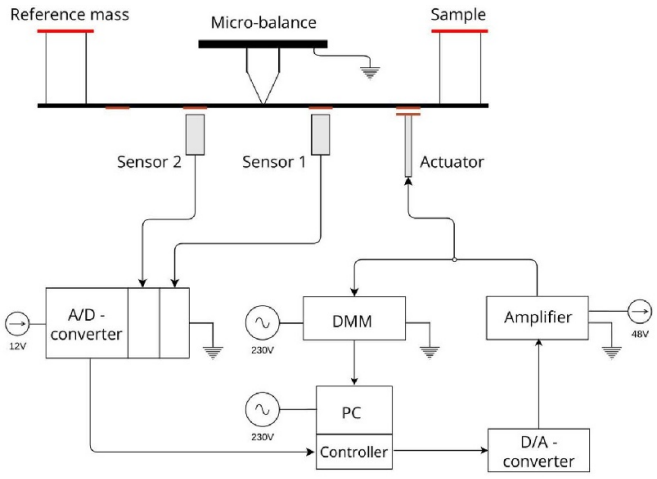


Figure C.9. Control system to maintain the microbalance in its null position using an actuator with capacitive plates to apply an electrically induced force. The actuator is installed only on the right side of the rotating beam. Measurements from the capacitive sensors are converted to digital signals and processed by a LabVIEW-programmed controller. The controller's output is converted back to an analog signal, amplified, and then applied to the actuator. The actuator voltage is precisely measured using a Digital Multimeter (DMM).

ORCID iD

J P M Hoefnagels https://orcid.org/0000-0001-8359-7575

References

[1] Mirshojaeian Hosseini M J and Nawrocki R A 2021 A review of the progress of thin-film transistors and their technologies for flexible electronics *Micromachines* **12** 655
[2] Herickhoff C D and van Schaijk R 2023 cMUT technology developments *Z. Med. Phys.* **33** 256–66
[3] Gupta S, Navaraj W T, Lorenzelli L and Dahiya R 2018 Ultra-thin chips for high-performance flexible electronics *npj Flex. Electron.* **2** 1–17
[4] Makhlouf A S H and Tiginyanu I 2011 *Nanocoatings and Ultra-Thin Films: Technologies and Applications* (Elsevier)
[5] Dennard R H, Cai J and Kumar A 2018 A perspective on today's scaling challenges and possible future directions *Handbook of Thin Film Deposition* 4th edn, ed K Seshan and D Schepis (William Andrew Publishing) pp 3–18
[6] Simon A H 2018 Chapter 7 - Sputter processing *Handbook of Thin Film Deposition* 4th edn, ed K Seshan and D Schepis (William Andrew Publishing) pp 195–230
[7] Chow L A 2018 Chapter 9 - Equipment and manufacturability issues in chemical vapor deposition processes *Handbook of Thin Film Deposition* 4th edn, ed K Seshan and D Schepis (William Andrew Publishing) pp 269–316
[8] Muneshwar T, Miao M, Borujeny E R and Cadien K 2018 Chapter 11 - Atomic layer deposition: fundamentals, practice and challenges *Handbook of Thin Film Deposition* 4th edn, ed K Seshan and D Schepis (William Andrew Publishing) pp 359–77
[9] Chan K and Gleason K K 2006 A mechanistic study of initiated chemical vapor deposition of polymers: analyses of deposition rate and molecular weight *Macromolecules* **39** 3890–4
[10] Scharf T and Krebs H 2002 Influence of inert gas pressure on deposition rate during pulsed laser deposition *Appl. Phys.* A **75** 551–4
[11] Chowdhury M A, Nuruzzaman D M and Rahaman M L 2011 The effect of gas flow rate on the thin film deposition rate on carbon steel using thermal CVD *Int. J. Chem. React. Eng.* **9** 73
[12] Priestland C R D and Hersee S D 1972 The effects of pressure on the deposition rate in rf sputtering processes *Vacuum* **22** 103–6
[13] Behrndt K H and Love R W 1962 Automatic control of film-deposition rate with the crystal oscillator for preparation of alloy films *Vacuum* **12** 1–9
[14] Park H-W, Park K, Kwon J-Y, Choi D and Chung K-B 2017 Effect of active layer thickness on device performance of tungsten-doped InZnO thin-film transistor *IEEE Trans. Electron Devices* **64** 159–63
[15] Pons-Flores C A *et al* 2017 Influence of active layer thickness, device architecture and degradation effects on the contact resistance in organic thin film transistors *Super. Vacio* **30** 46–50
[16] Khandelwal K, Shankar S S, Malhotra P, Biswas S, Panghal A, Roy S S and Sharma G D 2023 Unraveling the impact of thickness on active layer morphology and device performance of semitransparent organic solar cells: a comprehensive study *ACS Appl. Energy Mater.* **6** 10078–87
[17] Park W, Park S, Mun Y, Lee D and Jang K-S 2023 Effects of thickness on flexibility and thermoelectric performance of free-standing Ag_2Se films *J. Ind. Eng. Chem.* **121** 142–8
[18] Gupta D and Hong Y 2010 Understanding the effect of semiconductor thickness on device characteristics in organic thin film transistors by way of two-dimensional simulations *Org. Electron.* **11** 127–36
[19] Chatterjee S and Bhardwaj R 2023 A short review on optical interferometry techniques for characterization of a thin liquid film on a solid surface *Sadhana* **48** 30
[20] Boettcher T, Gronle M and Osten W 2017 Multi-layer topography measurement using a new hybrid single-shot technique: chromatic confocal coherence tomography (CCCT) *Opt. Express* **25** 10204
[21] Liu C, Erdmann J, Maj J and Macrander A 1999 Thickness determination of metal thin films with spectroscopic ellipsometry for x-ray mirror and multilayer applications *J. Vac. Sci. Technol.* A **17** 2741–8
[22] Hirayama T, Torii T, Konishi Y, Maeda M, Matsuoka T, Inoue K, Hino M, Yamazaki D and Takeda M 2012 Thickness and density of adsorbed additive layer on metal surface in lubricant by neutron reflectometry *Tribol. Int.* **54** 100–5
[23] R F Walker Ed 1962 Vacuum microbalance techniques *Proc. of the 1961 Conf. Held at the National Bureau of Standards, (Washington, D. C., 20 April–21 April)* vol 2 (Springer)
[24] Behrndt K 1962 Vacuum microbalance techniques *Proc. 1962 Conf. Held at Los Angeles* vol 3 (Plenum Press)
[25] Czanderna A W and Wolsky S P 1980 Microweighing in vacuum and controlled environments *Methods and Phenomena, Their Applications in Science and Technology* vol 4, ed A W Czanderna and S P Wolsky (Elsevier Scientific Pub. Co.)
[26] Alassi A, Benammar M and Brett D 2017 Quartz crystal microbalance electronic interfacing systems: a review *Sensors* **17** 2799
[27] Buttry D A and Ward M D 1992 Measurement of interfacial processes at electrode surfaces with the electrochemical quartz crystal microbalance *Chem. Rev.* **92** 1355–79
[28] Wajid A 1997 On the accuracy of the quartz-crystal microbalance (QCM) in thin-film depositions *Sens. Actuators* A **63** 41–46

[29] Stanford Research Systems 2005 QCM 100-quartz crystal microbalance theory and calibration (available at: www.lambdaphoto.co.uk/pdfs/SRS/LAMBDA_Quartz%20Crystal%20Microbalance%20Theory.pdf)
[30] Heusler K E, Grzegorzewski A, Jäckel L and Pietrucha J 1988 Measurement of mass and surface stress at one electrode of a quartz oscillator *Ber. Bunsenges. Phys. Chem.* **92** 1218–25
[31] Pletea M, Brückner W, Wendrock H and Kaltofen R 2005 Stress evolution during and after sputter deposition of Cu thin films onto Si (100) substrates under various sputtering pressures *J. Appl. Phys.* **97** 054908
[32] Chason E Resolution and sensitivity of stress measurements with the k-Space Multi-beam Optical Sensor (MOS) system (available at: www.k-space.com/pdfs/kSA_MOS_Resolution.pdf)
[33] Abadias G *et al* 2018 Review article: stress in thin films and coatings: current status, challenges and prospects *J. Vac. Sci. Technol.* A **36** 020801
[34] Freund L B and Suresh S 2004 *Thin Film Materials: Stress, Defect Formation and Surface Evolution* (Cambridge University Press)
[35] Swann M The principles of QCM-I quartz crystal microbalance with impedance analysis (available at: https://mmrc.caltech.edu/Gamry/manuals/QCM-I-principles.pdf)
[36] Thundat T, Oden P I and Warmack R J 1997 Microcantilever sensors *Microscale Thermophys. Eng.* **1** 185–99
[37] Raiteri R, Grattarola M, Butt H-J and Skládal P 2001 Micromechanical cantilever-based biosensors *Sens. Actuators* B **79** 115–26
[38] Shao J Y 2001 Measuring piconewton forces and its application in cellular and molecular biomechanics *Advances in Biomechanics* (*Beijing China*, *2001*)
[39] Alvarez M, Zinoviev K, Moreno M and Lechuga L M 2008 Chapter 10 - Cantilever biosensors *Opt. Biosens.* 419–52
[40] Griffiths D 1961 Robust helical spring microbalance *J. Sci. Instrum.* **38** 463
[41] Schwoebel R L 1980 Chapter 2 - Beam microbalance design, construction and operation *Methods and Phenomena* (*Microweighing in Vacuum and Controlled Environments*) vol 4, ed A W Czanderna and S P Wolsky (Elsevier) pp 59–93
[42] Hodsman G F 1951 Developments in microchemical balance design *Bericht Uber den I. Internationalen Mikrochemischen Congress: (Graz), (2 July–6 July 1950)* (*Mikrochemie Vereinigt mit Mikrochimica Acta*) ed M K Zacherl (Springer) pp 133–42
[43] Robens E, Jayaweera S A A and Kiefer S 2014 Balances *Balances: Instruments, Manufacturers, History* ed E Robens, S A A Jayaweera and S Kiefer (Springer) pp 141–271
[44] Evans E L, Thomas J M and Williams B R 1966 The construction of a robust metal vacuum microbalance *J. Sci. Instrum.* **43** 263
[45] Marangoni R R, Rahneberg I, Hilbrunner F, Theska R and Fröhlich T 2017 Analysis of weighing cells based on the principle of electromagnetic force compensation *Meas. Sci. Technol.* **28** 075101
[46] Arumugam K and Shaw G 2023 Perspective on small mass and force measurements *Meas. Sci. Technol.* **34** 081002
[47] (Available at: www.mt.com/int/en/home/products/Laboratoryweighingsolutions/microbalances.html)
[48] (Available at: www.sartorius.com/en/products/weighing/laboratory-balances/micro-lab-balance)
[49] Information from research engineers of Mettler Toledo
[50] (Available at: https://pim-resources.coleparmer.com/catalog-page/gy44-0042.pdf)
[51] Tallant D and Taylor E 1980 Chemical analysis of thin films at Sandia National Laboratories *Technical Report* United States, sAND–80-0605 INIS Reference Number: 11564343
[52] (Available at: www.plasmaetch.com/plasma-cleaning-systems.php)
[53] Martens R Novel diagnostics to assess stress-depth profiles and mechanics in multi-layer thin films (available at: https://research.tue.nl/en/publications/novel-diagnostics-to-assess-stress-depth-profiles-and-mechanics-i)
[54] Carey W, Wiebe A, Nord R and Altgilbers L 2011 Characterization of Paschen curve anomolies at high PD values *2011 IEEE Pulsed Power Conf.* (IEEE) pp 741–4
[55] Young W and Budynas R 2001 *Roark's Formulas for Stress and Strain* MacGraw-Hill international edn (McGraw Hill LLC)
[56] Kuriakose S and Shunmugam M S 2004 Characteristics of wire-electro discharge machined Ti6Al4V surface *Mater. Lett.* **58** 2231–7
[57] Mondal A, Roy P and Mitra S 2021 Experimental investigation on electro discharge machining of Ti6Al4V alloy *Adv. Mater. Process. Technol.* **7** 262–72
[58] Mohd Abbas N, Solomon D G and Fuad Bahari M 2007 A review on current research trends in electrical discharge machining (EDM *Int. J. Mach. Tools Manuf.* **47** 1214–28
[59] Ho K H and Newman S T 2003 State of the art electrical discharge machining (EDM) *Int. J. Mach. Tools Manuf.* **43** 1287–300
[60] 2003 Mails from Engineers of Micro-Epsilon (available at: www.micro-epsilon.us/fileadmin/download/products/catcapaNCDTen-us.pdf)
[61] Webster J G and Eren H 2014 Chapter 25: Capacitive sensors *Measurement, Instrumentation and Sensors Handbook* (*Spatial, Mechanical, Thermal and Radiation Measurement*) 2nd edn (CRC Press)
[62] Conrads H and Schmidt M 2000 Plasma generation and plasma sources *Plasma Sources Sci. Technol.* **9** 441–54
[63] Brooks C B, Buie M J and Vaidya K J 1998 Plasma process induced surface damage removal *J. Vac. Sci. Technol.* A **16** 260–4
[64] Barna A, Pécz B and Menyhard M 1998 Amorphisation and surface morphology development at low-energy ion milling *Ultramicroscopy* **70** 161–71
[65] Mohith S, Upadhya A R, Navin K P, Kulkarni S M and Rao M 2020 Recent trends in piezoelectric actuators for precision motion and their applications: a review *Smart Mater. Struct.* **30** 013002
[66] Yoon K-T, Park S-R and Choi Y-M 2020 Electromagnetic force compensation weighing cell with magnetic springs and air bearings *Meas. Sci. Technol.* **32** 015905
[67] Gast T 1986 Development of the magnetic suspension balance *Measurement* **4** 53–62
[68] Addiss R 1958 The stability of solitary waves *PhD Thesis* Cornell University
[69] University of Pennsylvania 1958 Electric forces between charged plates (available at: www-eng.lbl.gov/shuman/XENON/REFERENCES&OTHER_MISC/electric_forces.pdf)
[70] Zhu T and Ye W 2010 Origin of Knudsen forces on heated microbeams *Phys. Rev.* E **82** 036308
[71] Nabeth J, Chigullapalli S and Alexeenko A 2010 What determines knudsen force at the microscale *AIP Conf. Proc.* vol 1333 pp 754–9
[72] Akbarov S D 2007 Recent investigations on dynamic problems for an elastic body with initial (residual) stresses (review) *Int. Appl. Mech.* **43** 1305–24